CHAPTER 5 CRESCENT SHAPED UWB DIPOLE ANTENNA

5.1   Introduction

From the literature survey, it is found that the impedance matching complexity faced while designing monopole or fractal antenna structure can be resolved or minimized by designing dipole antenna structures as they have large input impedance. This large value of input impedance makes the impedance matching easier. Another advantage of dipole antenna structures is that they have omnidirectional radiation patterns as desired for UWB communication. The only disadvantage with dipole structures is that their size gets increased.

This chapter presents the design and analysis of crescent shaped dipole antenna configuration for UWB applications. The frequency domain and time domain analysis are done by using HFSS [477] and CST MWS [478] respectively. Their techniques and features are already discussed in chapter three.

5.2   Antenna Design

A compact crescent shaped dipole antenna for UWB applications is designed. The techniques of loading the radiator with notch and modified feedline are utilized to achieve the designed antenna structure with an ultra wide bandwidth.

The geometry of the designed antenna structure is shown in Figure 5.1. The optimized dimensions of the designed antenna structure are listed in Table 5.1. The designed antenna structure is etched on a FR-4 epoxy substrate having dielectric constant, ε_r=4.4, loss tangent tan δ=0.02 and a thickness of h=1.6mm. The radiator and the feedline are printed on both sides of the substrate. A stepped microstrip line comprising of five rectangular subsections is utilized to feed the crescent shaped radiator. Each subsection of the feedline has different length and width. Maximum

impedance is achieved for the subsection having minimum width and vice versa. Due to the stepped structure of feedline, there is a smooth transition between the input impedance of dipole antenna and the impedance of coaxial probe. The crescent shape of the radiator is derived by loading an elliptical radiator with semi-elliptical notch along its major axis. The dimensions of each subsection of the stepped feedline, crescent radiator and truncated rectangular ground plane are optimized. The location of the elliptical notch is also optimized. The optimization of antenna structure dimensions is done by varying one parameter and fixing the others. The truncation of ground plane created a capacitive load to neutralize the inductive nature of the patch producing nearly pure resistive input impedance. Due to this pure resistive input impedance, impedance matching between the patch and the feedline got improved in a wide range of frequencies.

Table 5.1 Optimized dimensions of the crescent dipole antenna

Parameter	Dimension (mm)	Parameter	Dimension (mm)
L_{sub}	34	W_{sub}	41
L_1	5.4	W_1	2.6
L_2	4.6	W_2	2.8
L_3	12.8	W_3	2.4
L_4	2.4	W_4	1.6
L_5	0.7	W_5	0.75
a	5.25	b	6
c	3	d	4
L9	0	W8	10
L_g	6.8	h	1.6
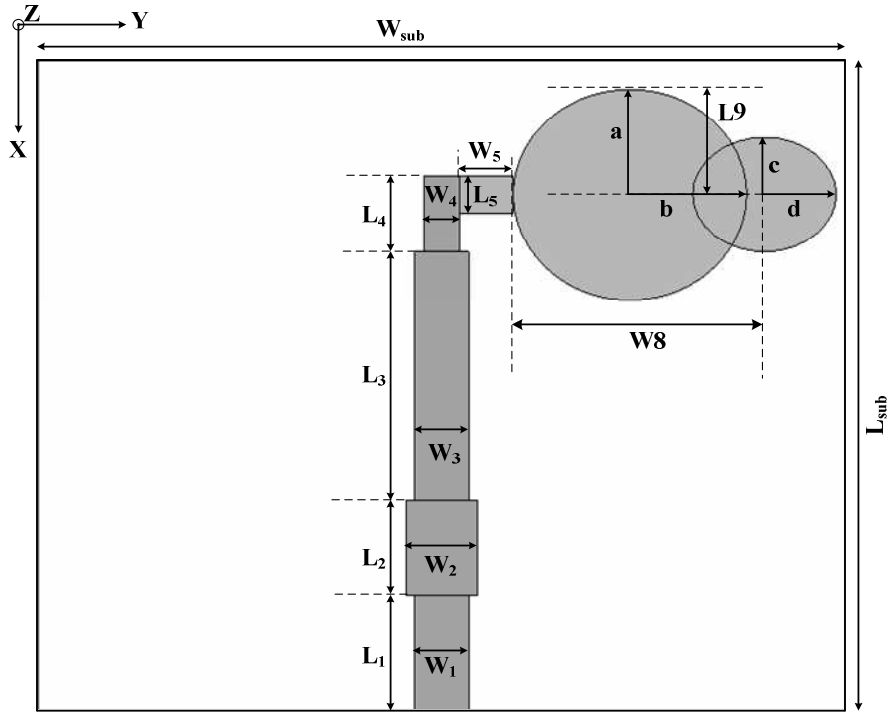
(a) Top View
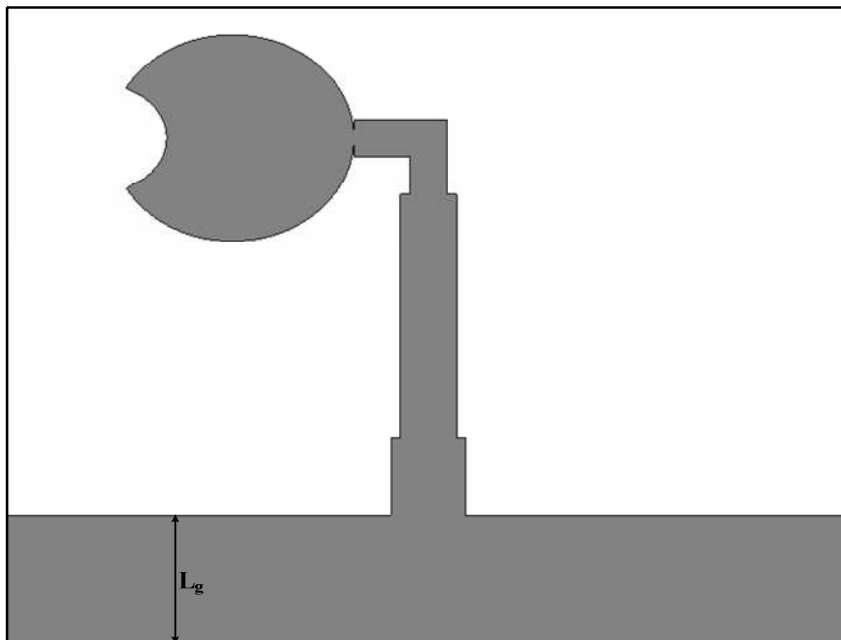
(b) Bottom View

Figure 5.1 Geometry of the crescent dipole antenna.

(a) Triangular　　　　　　　　　(b) Rectangular

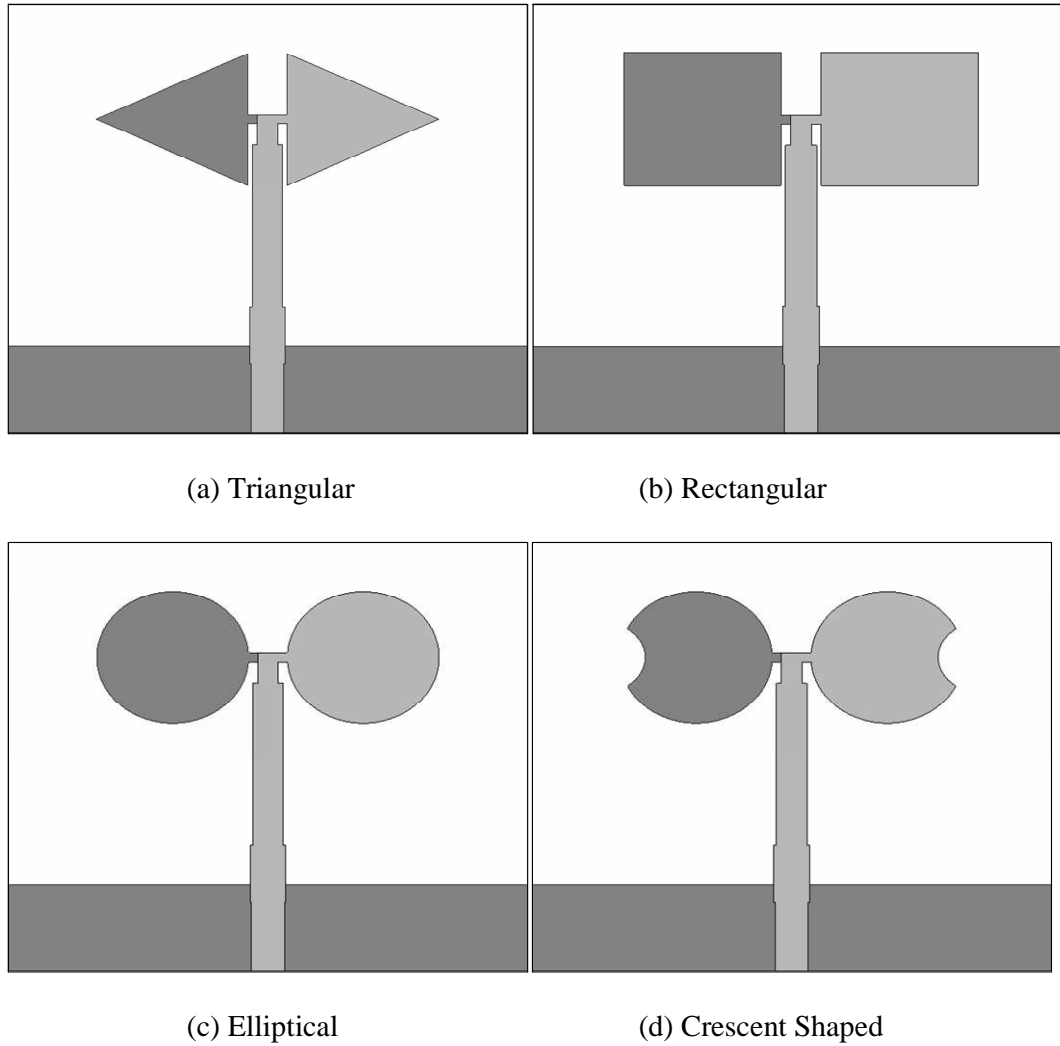(c) Elliptical　　　　　　　　　(d) Crescent Shaped

Figure 5.2 Different shapes of the radiating elements in dipole antenna.

5.3 Results and Discussion

In this section, various frequency and time domain results are discussed and analyzed. These results include reflection coefficient characteristic, input impedance characteristic, radiation patterns, peak gain, efficiency and parametric analysis results in frequency domain. In time domain analysis subsection, the results like group delay, fidelity factor, isolation magnitude and phase to prove the suitability of the designed antenna for UWB applications are discussed.

5.3.1 Reflection Coefficient versus Frequency Characteristics

The comparison between the reflection coefficient versus frequency characteristics for different shapes of radiating elements, shown in Figure 5.2, is depicted in Figure 5.3 and listed in Table 5.2. From Figure 5.3 and Table 5.2, it is observed that the triangular radiating dipole element has four operating bands. On replacing the triangular dipole elements with rectangular elements, the antenna performance is improved and five operating bands are achieved with enhancement in the bandwidth of first operating band. On replacing the rectangular radiating element with elliptical element, two wide bands of operation are achieved. After loading the elliptical radiating element with semi-elliptical notch along its major axis, the reflection coefficient curve around 11 GHz shifted downward and resulted into a single wide operating band. The designed antenna structure has six resonances at the frequencies of 3.7, 7.7, 9.4, 11.6, 14.4 and 17.1 GHz. From Figure 5.3 and above discussion, it is concluded that the reflection coefficient performance of the antenna structure gets improved with increase in the number of edges of the radiating patch. This increase in the number of edges results into larger area of the radiating patch.

Table 5.2 Tabular comparison of performances of different radiating elements

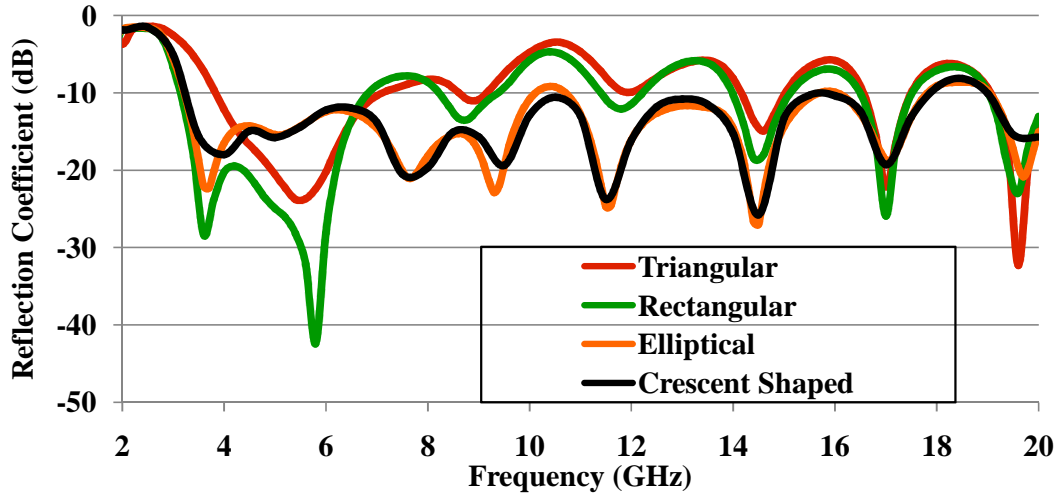| Configu-ration	Triangular		Rectangular		Elliptical		Crescent Shaped	
	f_L (GHz)	f_H (GHz)	f_L (GHz)	f_H (GHz)	f_L (GHz)	f_H (GHz)	f_L (GHz)	f_H (GHz)
BW I	3.82	7.14	3.08	6.9	3.18	10.16	3.28	17.85
BW II	-	-	8.17	9.44	10.68	17.88	-	-
BW III	-	-	11.36	12.29	-		-	-
BW IV	-	-	14	15.15	-		-	-
BW V	-	-	16.47	17.56	-		-	-

Figure 5.3 Variation of reflection coefficient with frequency for different radiating elements

The fabricated prototype of the designed antenna structure is shown in Figure 5.4. The experimental measurement of the variation of $|S_{11}|$ for the fabricated prototype is done by using the Anritsu's MS2038C VNA. The simulated and measured reflection coefficient plots for the designed antenna are shown in Figure 5.5. In Figure 5.5, the reflection coefficient versus frequency plot of the designed antenna obtained during the time domain analysis of the optimized antenna by using FIT based CST MWS is also presented. The band edge frequencies and bandwidth of the simulated and measured reflection coefficient plots are listed in Table 5.3. From Figure 5.5 and Table 5.3, it is observed that a good agreement is obtained between the simulated and measured results.
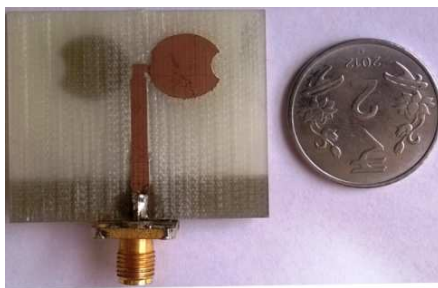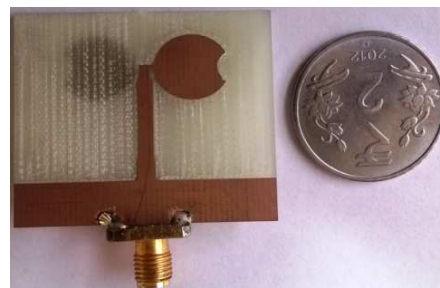
(a) Top View　　　　　　　　　　(b) Bottom View

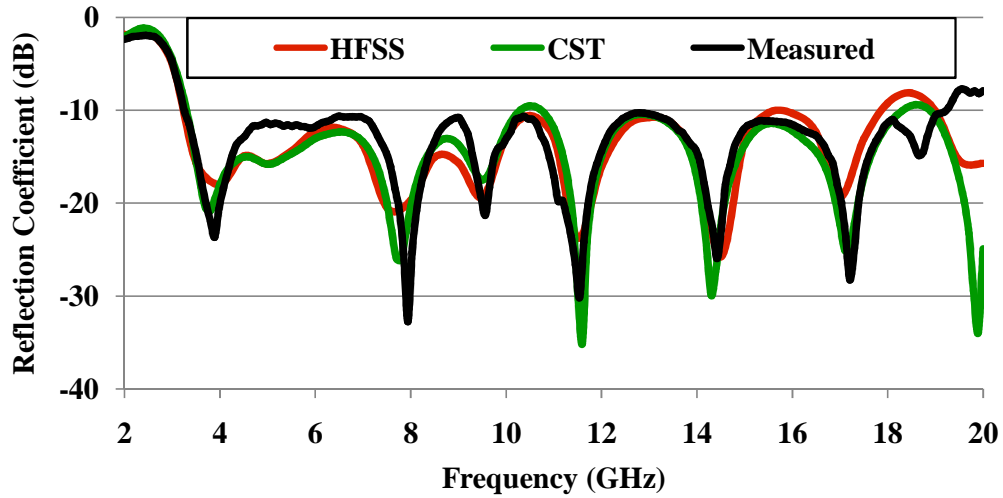Figure 5.4 Prototype of the crescent dipole antenna

Figure 5.5 Comparison of simulated and measured reflection coefficient versus frequency characteristics for crescent dipole antenna.

Table 5.3 Comparison of simulated and measured results of crescent dipole antenna

S. No.	Method	Lower cutoff, f_L(in GHz)	Higher cutoff, f_H(in GHz)	Bandwidth	
				In GHz	In %
1.	HFSS	3.28	17.85	14.57	137.9
2.	CST	3.29	18.32	15.03	139
3.	Measured	3.26	19.1	15.84	141.7

5.3.2 VSWR versus Frequency Characteristic

The simulated and measured VSWR plots of the designed antenna, presented in Figure 5.6, leads to the observations similar to that of reflection coefficient characteristics.
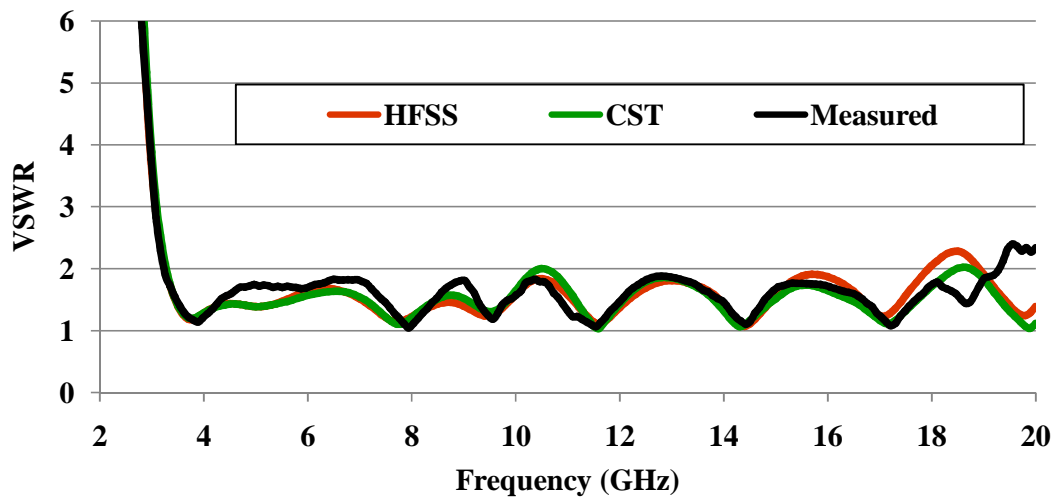

Figure 5.6 Comparison of simulated and measured VSWR versus frequency characteristics for crescent dipole antenna.

5.3.3   Input Impedance versus Frequency Characteristic

The variation of resistance and reactance of the input impedance for designed antenna with frequency are demonstrated in Figure 5.7. From Figure 5.7, it is observed that the resistance is oscillating around 50Ω whereas the reactance is varying around 0 Ω in the operating band. These observations lead to a conclusion that the overall input impedance of the designed antenna structure is approximately equal to the characteristic impedance of the coaxial probe i.e. 50Ω.
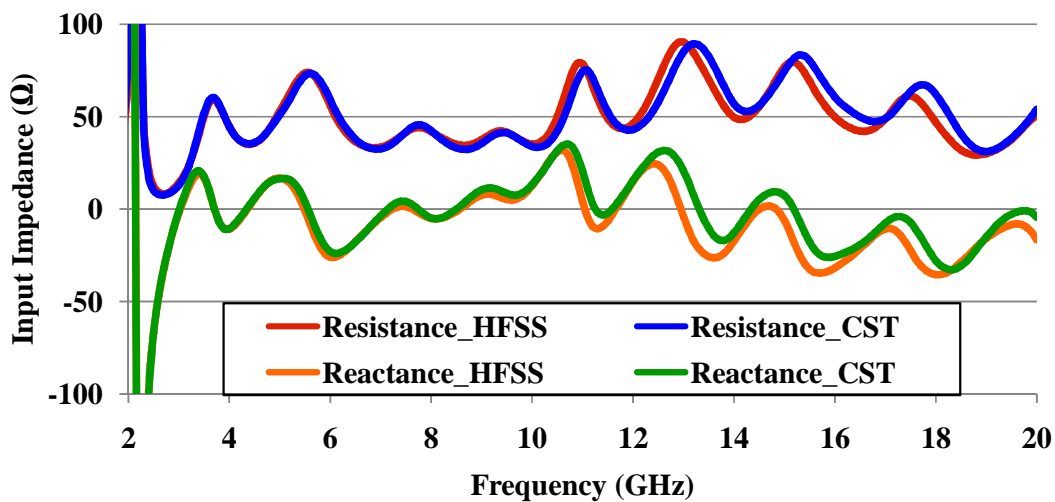
Figure 5.7 Variation of simulated resistance and reactance of the input impedance with frequency for crescent dipole antenna.

5.3.4   Surface Current Density Distribution

The simulated surface current distribution plots of the designed antenna structure at its six resonances are demonstrated in Figure 5.8(a)-(f). At the first resonance, Figure 5.8(a), the surface current is observed to be concentrated inside the feedline, ground plane, lower dipole element and left half of dipole element fed by the feedline. Zero or negligible current density is observed at the right half of the dipole element fed by the feedline. For the second resonance, Figure 5.8(b), the current is observed to be distributed uniformly along the whole antenna surface. In case of third resonance, Figure 5.8(c), uniform current distribution is observed along the antenna surface except

(a) 3.7 GHz

(b) 7.7 GHz
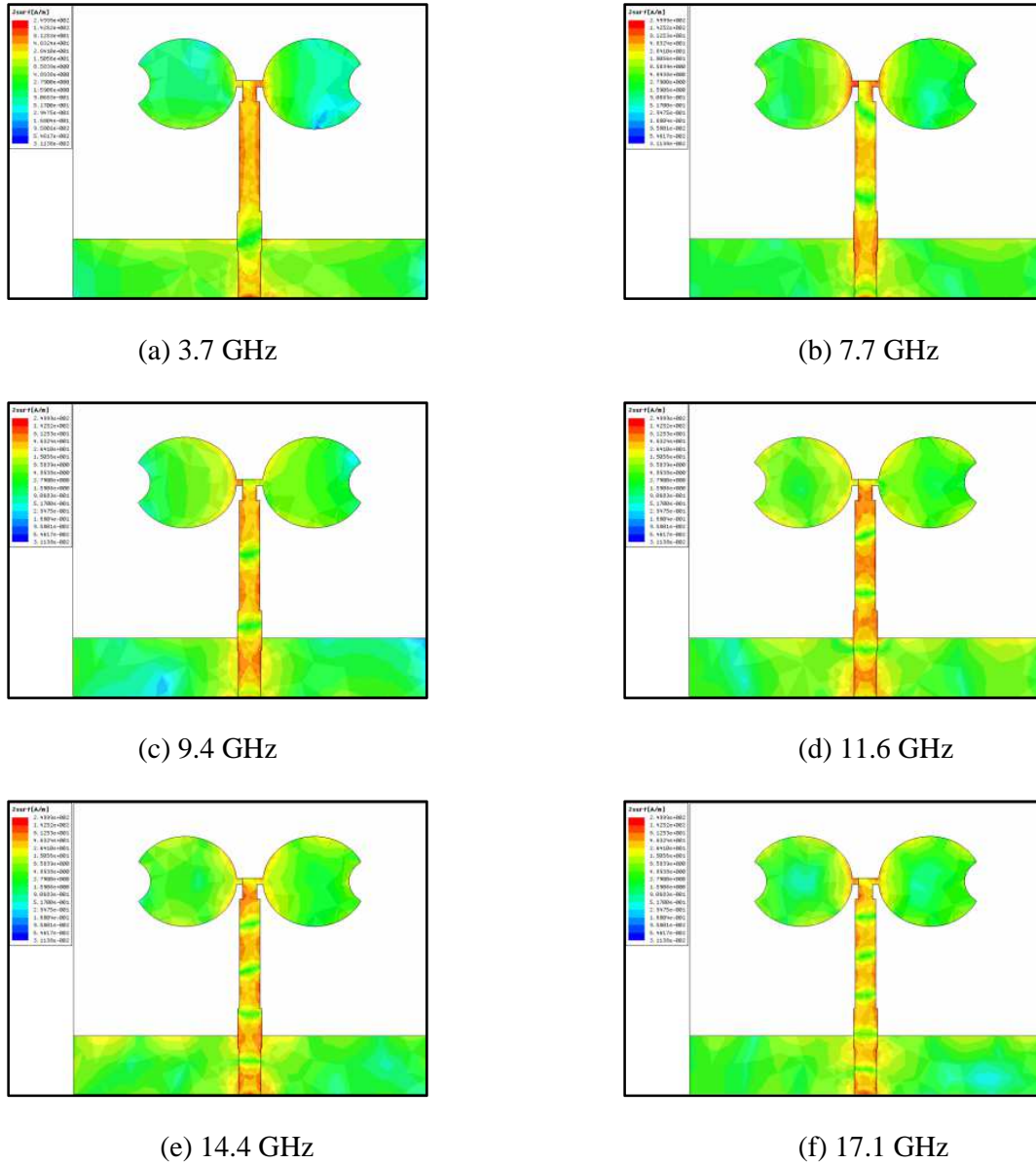
(c) 9.4 GHz

(d) 11.6 GHz

(e) 14.4 GHz

(f) 17.1 GHz

Figure 5.8 Simulated surface current density plots of the crescent dipole antenna at its six resonance frequencies.

around the semi-elliptical notches of dipole elements and quarter sections of ground plane at its extremities. At the fourth resonance, Figure 5.8(d), uniform distribution of surface current is observed along the antenna surface. Similar current distribution is observed for the fifth resonance, shown in Figure 5.8(e), with increase in the area of zero current density surface in the ground plane. In case of sixth resonance, depicted in

Figure 5.8(f), the distribution of current is unaltered along the antenna structure except small area of zero current density surfaces at the central portion of dipole elements.

5.3.5   Far Field Radiation Patterns

During the radiation pattern measurement setup, illustrated in Figure 5.9, the antenna structure is placed along the *X*-axis, pointing in the direction of $\Phi=0°$ and located in the *X–Y* plane. The θ is varied from $\theta=0°$ to $360°$ to measure the E-plane and H-plane patterns in the *X–Z* plane and *Y–Z* plane respectively.
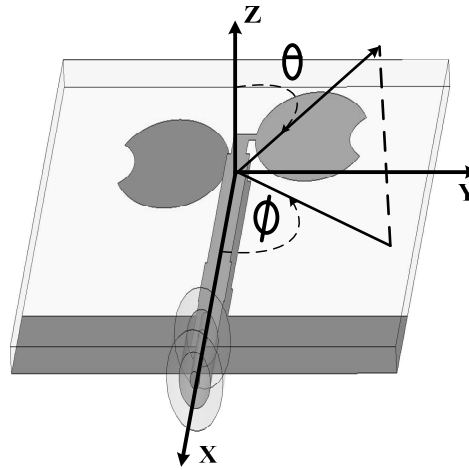
Figure 5.9 Radiation pattern measurement setup for crescent dipole antenna

The simulated and measured radiation patterns of the designed antenna at its six resonances in both E- and H-planes are depicted in Figure 5.10. For the first resonance at the frequency of 3.7 GHz, shown in Figure 5.10(a), it is observed that the E-plane ($\Phi=0^{o}$) pattern is quasi omnidirectional whereas the H-plane ($\Phi=90^{o}$) pattern has figure of eight shape. In case of second resonance at 7.7 GHz, depicted in Figure 5.10(b), the bidirectional nature of the H-plane pattern started shifting towards the omnidirectional nature and the omnidirectional nature of the E-plane is negligibly distorted. At the third resonance of 9.4 GHz, demonstrated in Figure 5.10(c), the E-plane pattern got directional and the H-plane pattern has become nearly omnidirectional.

(a) 3.7 GHz

(b) 7.7 GHz

(c) 9.4 GHz

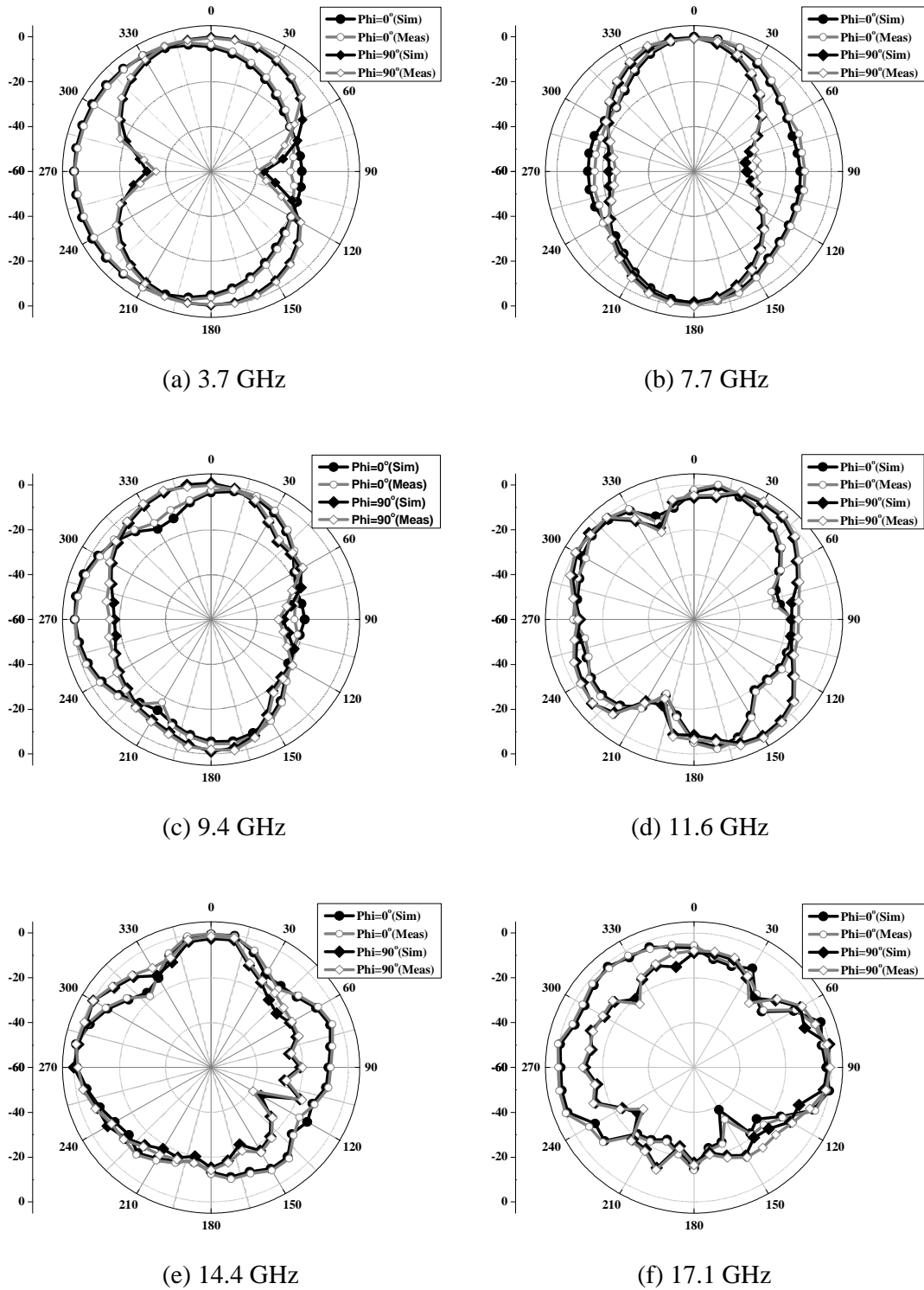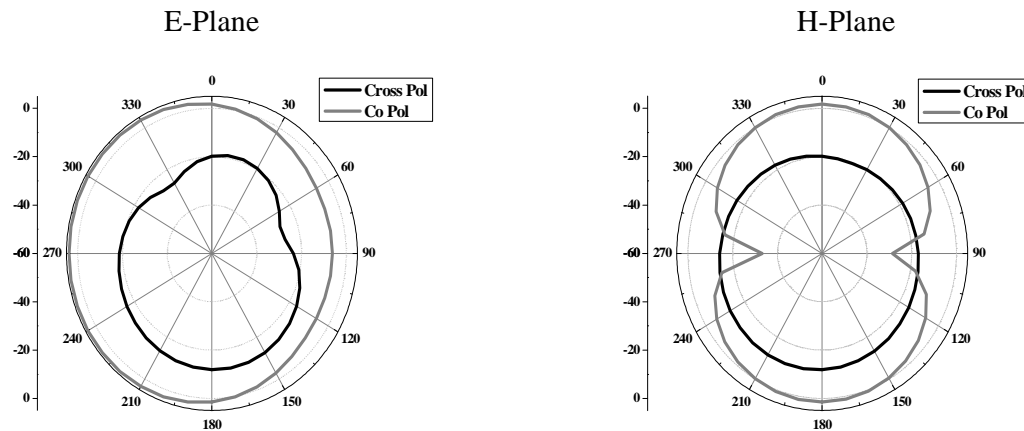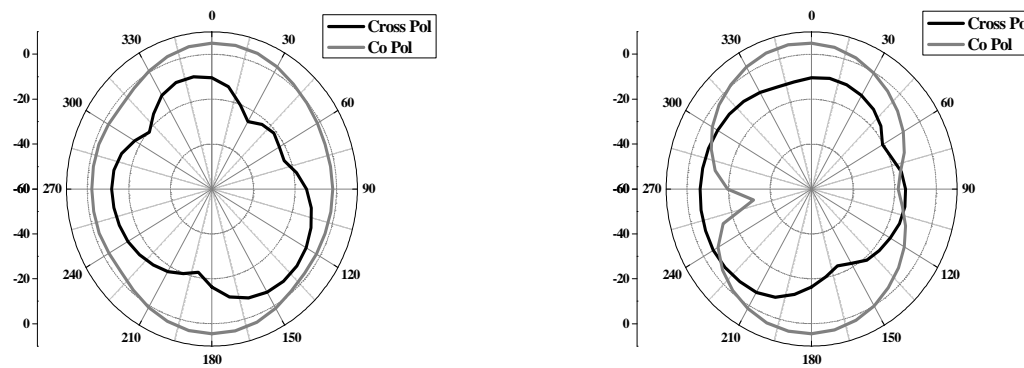(d) 11.6 GHz

(e) 14.4 GHz

(f) 17.1 GHz

Figure 5.10 Simulated and measured radiation patterns of the crescent dipole antenna at its six resonance frequencies

for the remaining three higher resonances at 11.6, 14.4 and 17.1 GHz, depicted in Figure 5.10(d)-(f), the radiation patterns in both planes are observed to be distorted omnidirectional in nature. The distortions in the radiation patterns at higher frequencies can be attributed to the excitation of higher modes at higher frequencies.
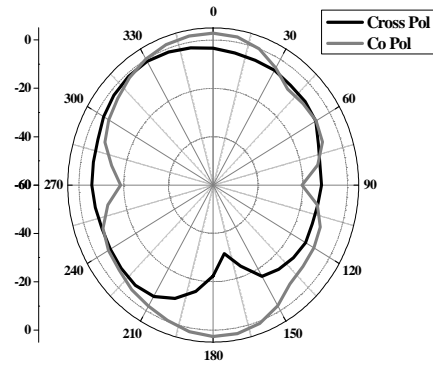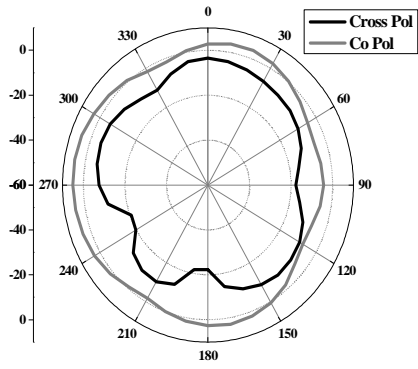
The measured co- and cross-polar radiation patterns at all six resonances in both E- and H-planes are depicted in Figure 5.11. Figure 5.11(a)-(f) show that at lower frequencies (<10 GHz), the cross polar level is lower than co-polar patterns for E-plane while for H-plane the levels of two patterns are comparable. At higher frequencies (>10 GHz), depicted in Figure 5.11(g)-(l), the level of cross-polar patterns is either comparable or higher than co-polar level in both planes which may be attributed to the excitation of hybrid modes at higher frequencies
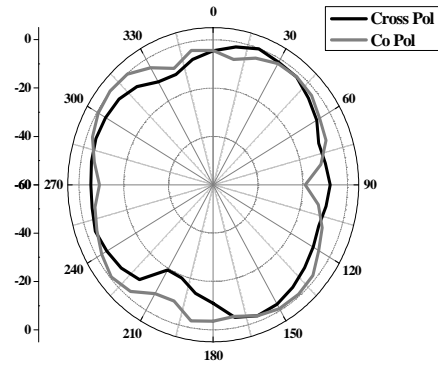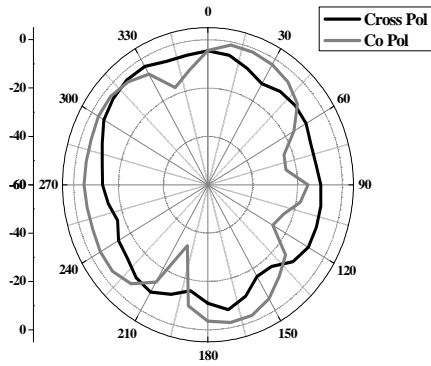
E-Plane   H-Plane
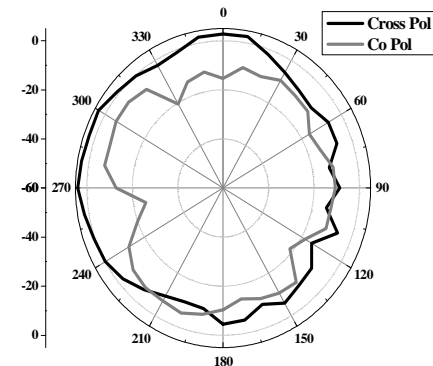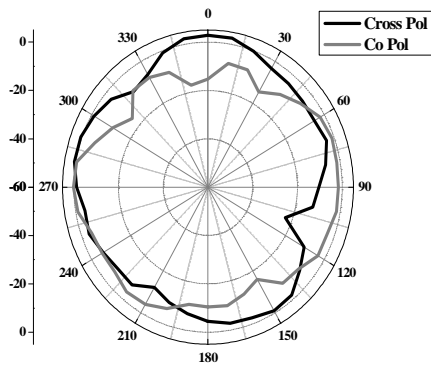

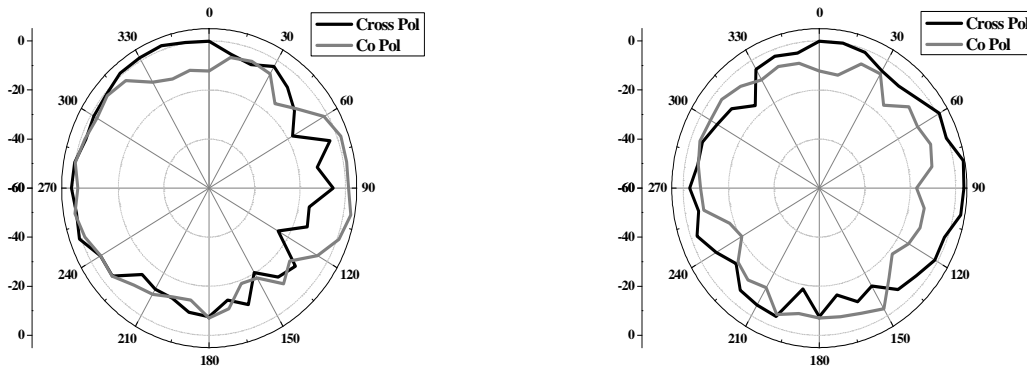(a) 3.7 GHz

(b) 7.7 GHz

(c) 9.4 GHz

(d) 11.6 GHz

(e) 14.4 GHz

(f) 17.1 GHz

Figure 5.11 Measured co- and cross-polar radiation patterns of the crescent dipole antenna at its six resonance frequencies in both E- and H-planes.

5.3.6 Gain and Efficiency Characteristics

The variation of measured peak realized gain with frequency for designed antenna is demonstrated in Figure 5.12. It is observed that the peak realized gain is varying between a maximum of 4.85 dB and a minimum of 1.08 dB with an average of 3.5 dB over the entire operating frequency band.
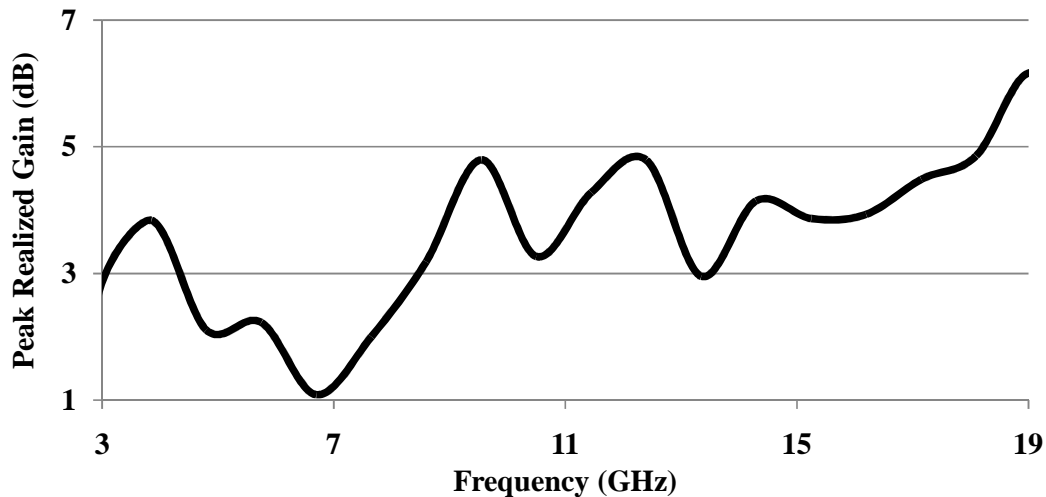

Figure 5.12 Variation of measured peak realized gain with frequency for the crescent dipole antenna

The simulated total efficiency and radiation efficiency versus frequency plots for the designed antenna structure are shown in Figure 5.13. Figure 5.13 shows that the total efficiency has its variation between 59% and 91%. It is also observed that the radiation efficiency is varying between 67% and 93%. The antenna efficiency is observed to be decreasing with increase in frequency. This phenomenon is occurring due to the varying performances of the radiating structures, substrate materials and SMA connectors.
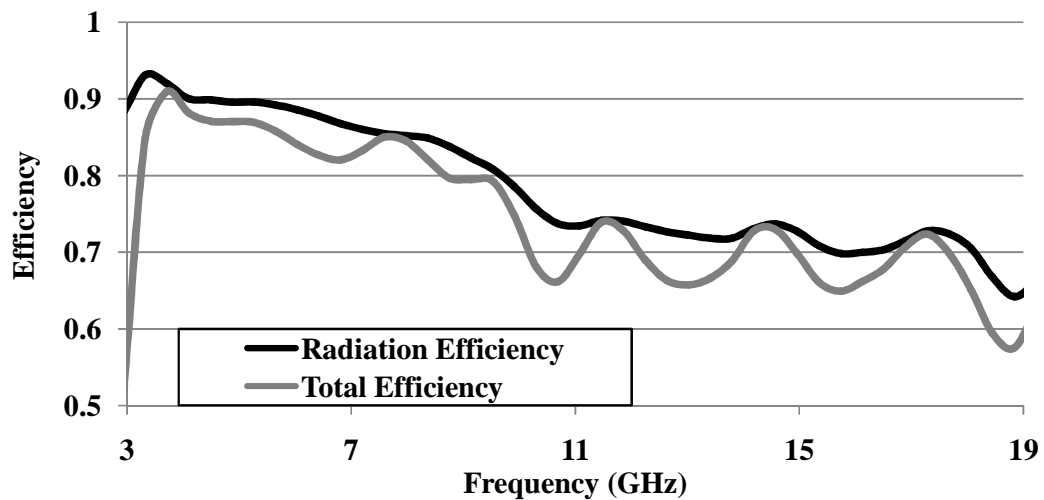

Figure 5.13 Variation of simulated total and radiation efficiencies with frequency for the crescent dipole antenna.

5.3.7   Time domain Analysis

The time domain analysis of the designed antenna structure is carried out by using CST MWS simulation tool. During the time domain analysis, two identical copies of the designed antenna structure are kept at a distance of 15 cm from each other in two configurations i.e. face to face and side by side, demonstrated in Figure 5.14. A Gaussian impulse is transmitted through each antenna structure and is received by the another antenna structure. The normalized amplitudes of the transmitted and received pulses for both configurations are presented in Figure 5.15. From these normalized

values of pulses, a predefined parameter i.e. Fidelity Factor is calculated by using the following equation for both configurations.

$$F = \frac{max}{\tau} \left\{ \left| \frac{\int s_t(t)s_r(t-\tau)d\tau}{\sqrt{\int s_t^2(t)dt}\sqrt{\int s_r^2(t)dt}} \right| \right\} \tag{55}$$

where, $s_t(t)$ and $s_r(t)$ are the excited and received pulses. The calculated values of fidelity factor for both configurations are listed in Table 5.4. From Table 5.4, it can be observed that an equal and good correlation is achieved between the transmitted and received pulses in both configurations.

The mathematical expression to define group delay is given in equation (47). Figure 5.16 shows that the simulated group delay of the designed antenna structure is varying from -1 to 1 ns for both configurations over the entire operating range. These values of the group delay are in the desired limits.
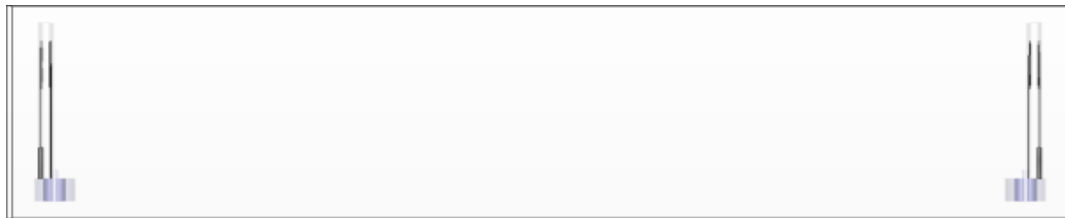
(a) Face to Face
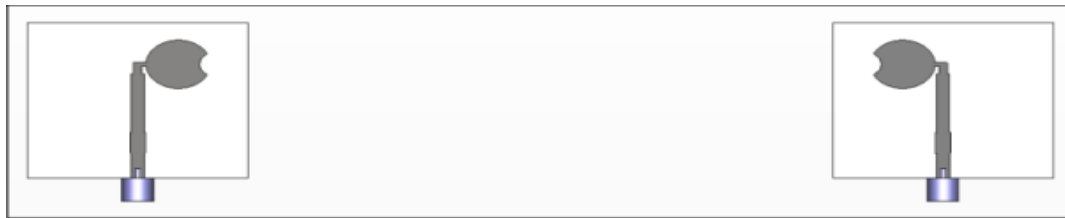
(b) Side by Side

Figure 5.14 Configurations of the crescent dipole antenna

Table 5.4 Fidelity factor(%) of the designed antenna structure in two configurations

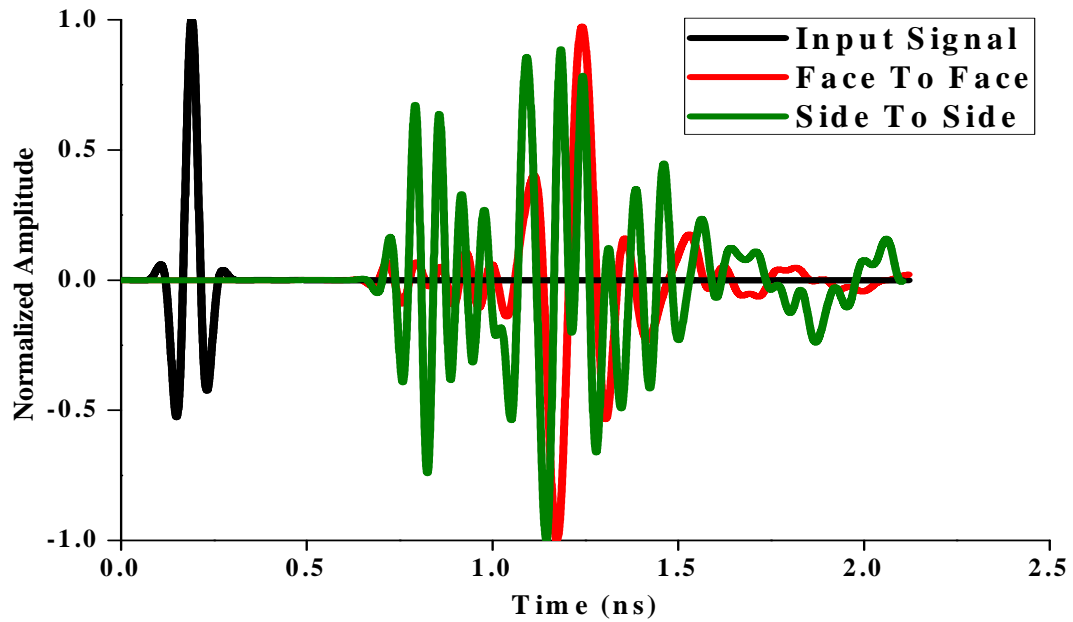| Configuration	Face To Face	Side By Side
Fidelity Factor (%)	61	59.5

Figure 5.15 Time domain analysis of the crescent dipole antenna
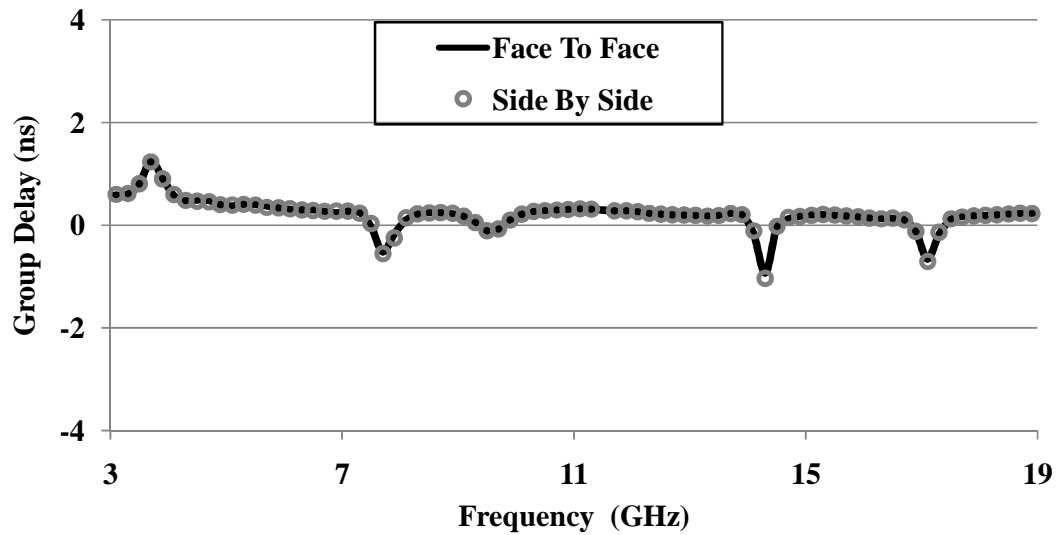
Figure 5.16 Variation of simulated group delay with frequency for the crescent dipole antenna in two configurations

The mathematical expression for transfer function is presented in equation (48). The variations of the simulated magnitude of isolation, $|S_{21}|$, in both configurations with respect to frequency are demonstrated in Figure 5.17. From Figure 5.17, it is observed that for side by side configuration the isolation is varying from -40 to -60 dB in the

frequency range of 3.3-13 GHz, -40 to -50 dB in the frequency band of 13-15 GHz and -35 to -45 dB in the frequency range of 15-17.85 GHz. For the face to face configuration, the isolation has its variation between -20 to -40 dB in the frequency band of 3.3-10.5 GHz and -40 to -60 dB for the frequency range of 10.5-17.85 GHz except a peak of -80 dB at 16.2 GHz. The simulated phase of the isolation for both configurations, shown in Figure 5.18, is observed to be varying linearly in the entire operating band. this linear variation of isolation phase indicates that there will be no out of phase component in the received pulse.
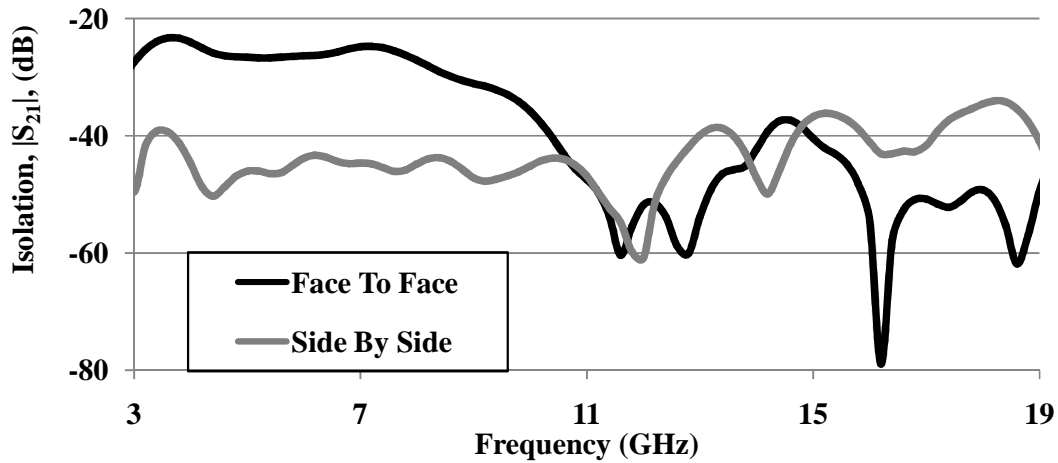

Figure 5.17 Variation of simulated magnitude of isolation, $|S_{21}|$, with frequency for the crescent dipole antenna in two configurations
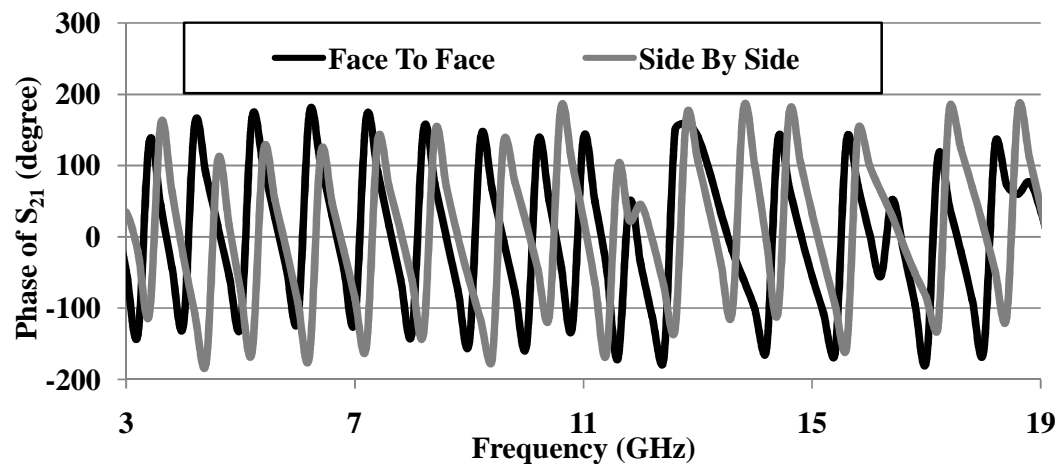

Figure 5.18 Variation of phase of simulated isolation, S_{21}, with frequency for the crescent dipole antenna in two configurations.

5.3.8   Parametric Analysis

This section deals with the effect of various parameters on the antenna performance.

5.3.8.1   Different Substrates

During the parametric analysis of the designed antenna structure, the default FR-4 epoxy substrate is replaced by two different substrate materials i.e. Carbon Nanotubes (CNT) [481] and $Ni_{0.2}Co_{0.2}Zn_{0.6}Fe_2O_4$ [482]. The reflection coefficient performances of the designed antenna structure for three substrate materials are shown in Figure 5.19. Figure 5.19 shows that for CNT three operating bands are achieved, whereas for $Ni_{0.2}Co_{0.2}Zn_{0.6}Fe_2O_4$ four bands are achieved. with enhanced bandwidth of first operating band. Table 5.5 demonstrates that the bandwidth of first operating band is maximum in case of FR4 substrate in comparison to that of other two substrates. The frequency ranges of three operating bands achieved in case of CNT material are 3.82-7.6 GHz, 9.39-12.8 GHz and 14.4-16.66 GHz. While for $Ni_{0.2}Co_{0.2}Zn_{0.6}Fe_2O_4$ substrate, the designed antenna has an operating range from 3.04-17.79 GHz with band-rejection in the frequency bands of 9.43-9.6 GHz, 13.82-15.47 GHz, 13.28-13.82 GHz and 15.47-16.63 GHz.
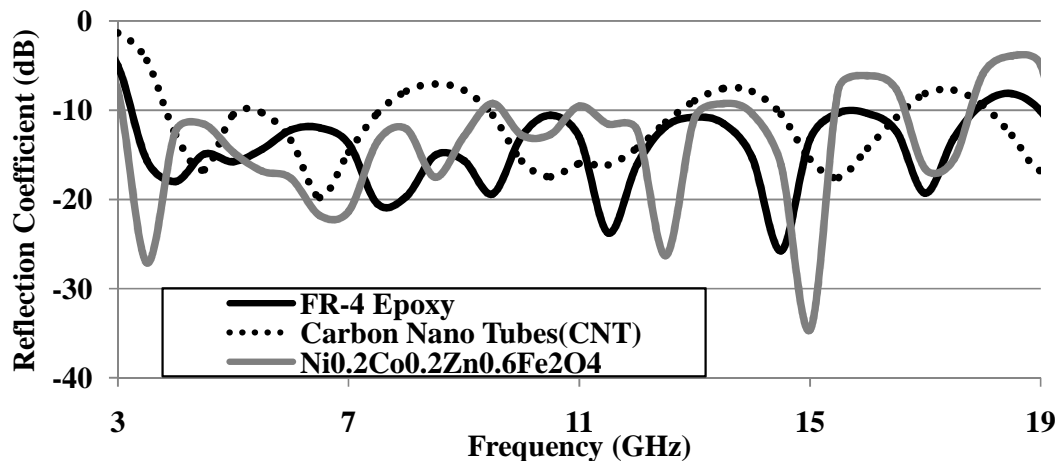

Figure 5.19 Reflection coefficient versus frequency characteristics of the crescent dipole antenna for three different substrate materials.

Table 5.5 Comparison of antenna performance for three different substrate materials

Substrate	FR-4	Carbon Nano Tubes	$Ni_{0.2}Co_{0.2}Zn_{0.6}Fe_2O_4$
ε_r	4.4	2.272	5.974
tan δ	0.02	0.0002	0.00226
f_L (GHz)	3.28	3.82	3.04
f_H (GHz)	17.85	7.6	9.43
BW_1 (GHz)	14.57	3.78	6.39
f_L (GHz)	-	9.39	9.6
f_H (GHz)	-	12.8	13.28
BW_2 (GHz)	-	3.41	3.68
f_L (GHz)	-	14.4	13.82
f_H (GHz)	-	16.66	15.47
BW_3 (GHz)	-	2.26	1.65
f_L (GHz)	-	-	16.63
f_H (GHz)	-	-	17.79
BW_4 (GHz)	-	-	1.16

5.3.8.2 Different thickness of Substrate, h

To study the effect of substrate height (h) on the performance of the designed antenna structure, it is varied from 0.8 to 2.4 mm. The variation of the reflection coefficient performance with change in the substrate height is demonstrated in Figure 5.20. It is observed that the antenna bandwidth is increased between the substrate thickness of 0.8 to 1.6 mm and afterwards it started decreasing.
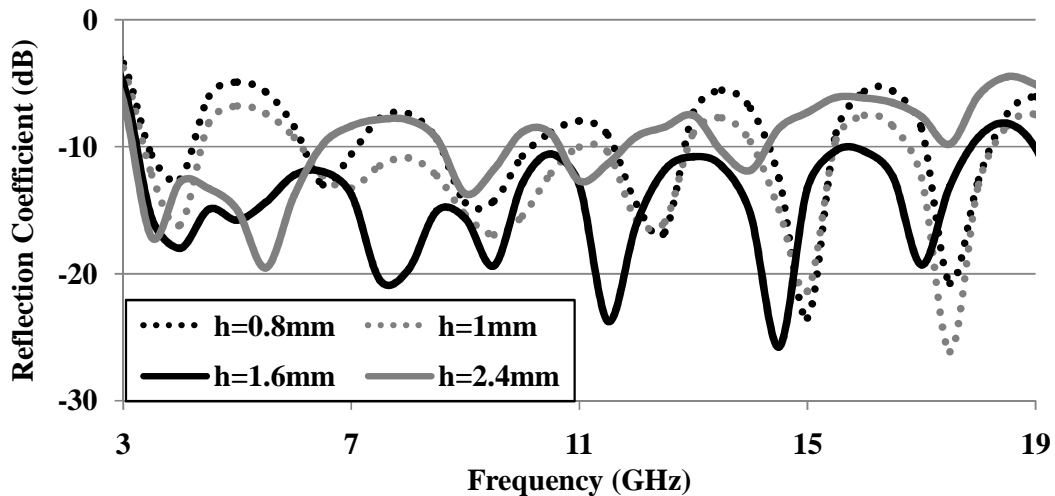

Figure 5.20 Simulated reflection coefficient versus frequency characteristics of the crescent dipole antenna for different thickness of substrate, h.

5.3.8.3 Major axis of elliptical slot, d

The reflection coefficient characteristics of the designed antenna structure for variations in the major axis of the elliptical notch, d, between 2 to 6 mm are shown in Figure 5.21. As shown in Figure 5.21, it is observed that the antenna performance is almost unaffected for the variation from 3 to 6 mm whereas for 2 mm the performance is slightly worse.
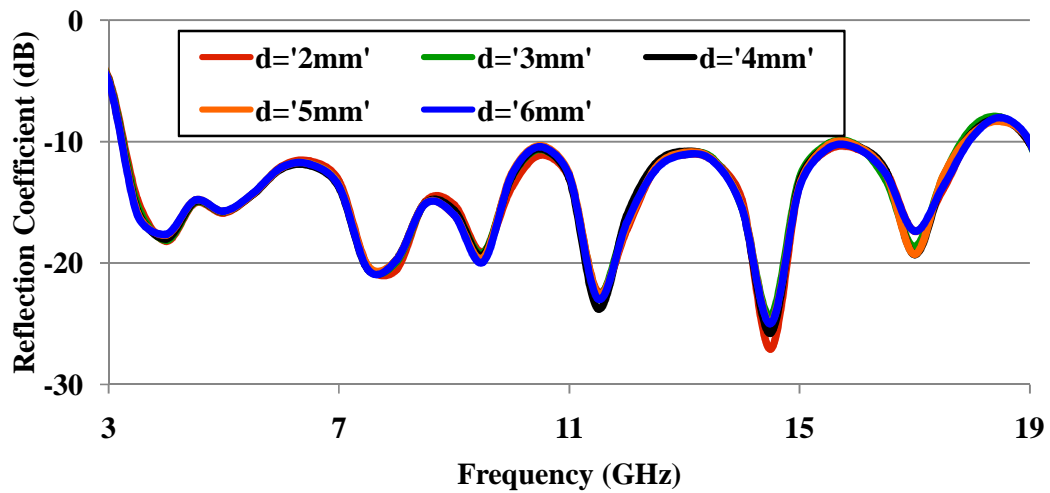

Figure 5.21 Simulated reflection coefficient versus frequency characteristics of the crescent dipole antenna for different values of major axis of elliptical slot.

5.3.8.4 Minor axis of elliptical slot, c

From Figure 5.22, the reflection coefficient curve of the designed antenna is observed to be shifting downwards around the frequency of 11 GHz for the variation of minor axis of elliptical notch, c, from 1 to 3 mm. For the variation between 3 to 5 mm, it is observed that the reflection coefficient plot is shifting upward i.e. towards -10 dB line, around the frequency of 15 GHz.
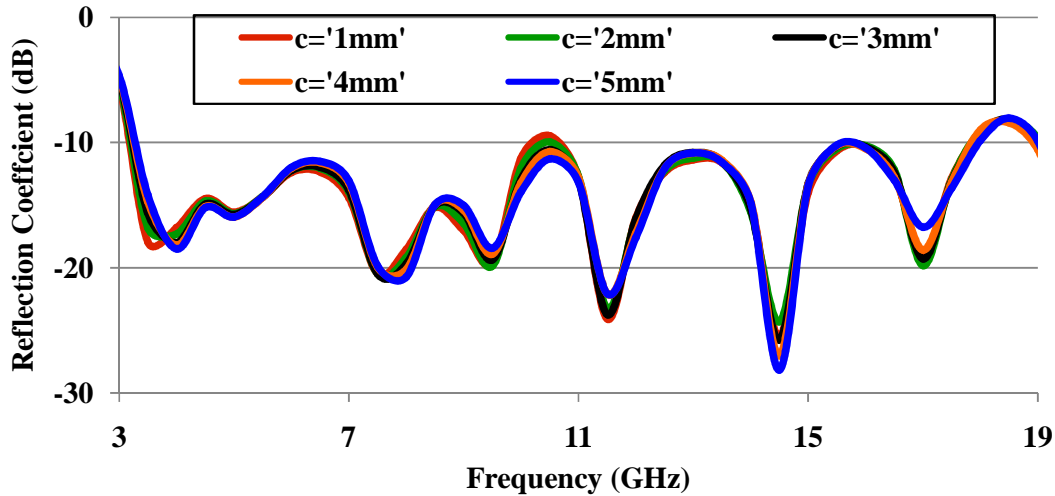
Figure 5.22 Simulated reflection coefficient versus frequency curves for different values of minor axis of elliptical slot.

5.3.8.5 Elliptical slot location along x-axis, L_9

The effect of elliptical notch movement along the negative x-axis, L_9, on the antenna's reflection coefficient performance is shown in Figure 5.23. Figure 5.23 shows that the reflection coefficient plot is shifting upward i.e. towards -10 dB line, with increase in the value of L_9 from 0 to 4 mm i.e. moving away from the major axis of the elliptical radiator.
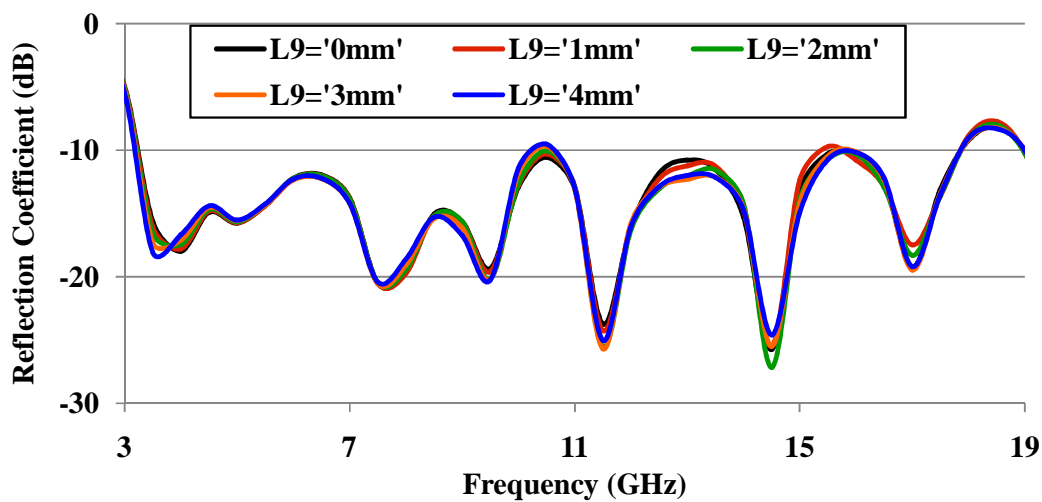

Figure 5.23 Simulated reflection coefficient versus frequency curves for variation in the elliptical slot location along x axis.

5.3.8.6   Elliptical slot location along y-axis, W_8

As demonstrated in Figure 5.24, the antenna performance is improving with elliptical notch movement in +y direction, W8, from 0 to 10 mm. From Figure 5.24, it is observed that for the variation of W8 from 0 to 4 mm, the reflection coefficient curve is providing two operating bands with a notch around 10.5 GHz and the lower edge of the first operating band is shifting towards higher frequency. At the value of 6 mm, the reflection coefficient curve is found to be shifting below and above -10 dB line at the frequencies of 10.5 GHz and 15.5 GHz respectively. Due to this shift in the reflection coefficient curves, the notch is shifted from 10.5 GHz to 15.5 GHz. It is also observed that for W8 equal to 6 mm, the lower edge of the first operating band is shifting from 3.25 GHz to 3.41 GHz. For values higher than 6 mm, the reflection coefficient curve is observed to be shifting towards -10 dB line at the frequencies of 10.5 GHz and 15.5 GHz. The lower band edge is also shifting towards the lower frequency. The maximum bandwidth of 14.57 GHz is achieved for the value of 10 mm.
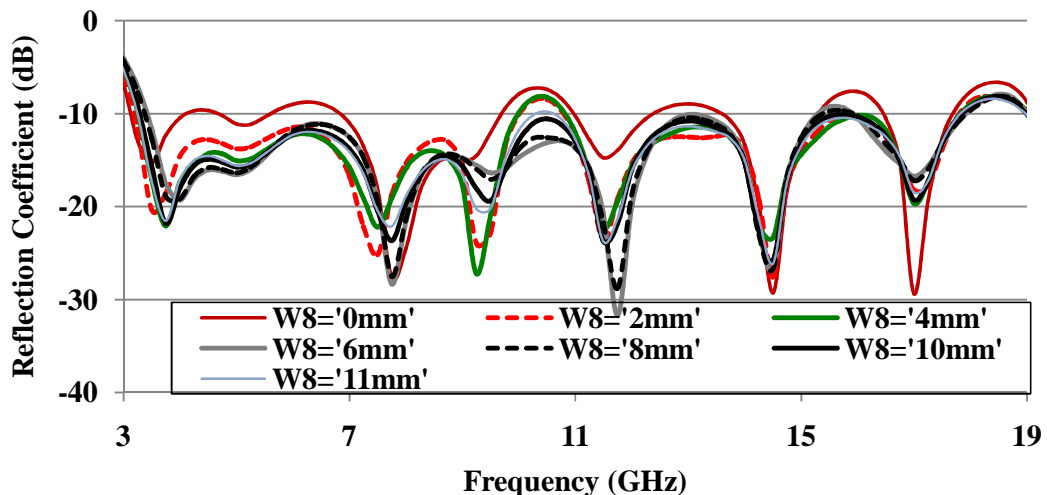

Figure 5.24 Simulated reflection coefficient versus frequency curves for variation in the elliptical slot location along y-axis.

5.3.9   Comparison with other structures

The designed antenna structure is compared to previously published dipole antenna structures [457, 450, 442, 443, 451, 428, 458] having nearly equal lower band edge frequency in terms of dimensions and impedance bandwidth. The quantitative comparison, listed in Table 5.6, indicates that for the designed antenna structure a typical reduction upto 84.46 % with a fractional bandwidth of 141% is achieved over other structures.

Table 5.6 Comparison of crescent shaped dipole with other dipole structures

Antenna	Bandwidth (GHz)	% BW	Size (mm^2)	% size reduction
[457]	3.06–12.21	119.84	40×35	0.43
[450]	3-11	114.29	48×46	36.87
[442]	2.95-11.76	119.78	48×46	36.87
[443]	3-12	120	46×48	36.87
[451]	3.656-15.64	124.21	49×53	46.32
[428]	3-11	114.29	71×86	77.17
[458]	3.3–20.7	145	115×78	84.46
designed antenna	**3.26-19.10**	**141.68**	**34×41**	**-**

A crescent shaped dipole antenna is investigated. The effect of different shapes of the radiator and different substrate materials on the antenna performance are also analyzed. The techniques of modified radiator and feedline are utilized to improve the impedance matching resulting into an impedance bandwidth of 3.26-19.1 GHz. The performance of the designed antenna for three different substrate materials is also presented. The size of the investigated antenna is also very compact as compared to dipole structures available in the literature. A good agreement is observed between the simulation and experimental results. The experimental results verified the suitability of investigated antenna structure for UWB applications. This antenna will find its applications for radiolocation (3.41 GHz), MFCN (3.4-3.8 GHz), BWA (3.4-3.8 GHz),

BBDR (4.940-4.990 GHz), Radio LANs (WAS/RLANs within the bands 5.15-5.35 GHz, 5.47-5.725 GHz and 17.1-17.3 GHz), ISM (5.725-5.875 GHz), BFWA (5.725-5.875 GHz), Mobile satellite applications (7.250-7.375 GHz), ITS (5.875-5.925 GHz and 5.855-5.875 GHz), radio determination applications (4.5-10.6 GHz, 13.4-14.0 GHz), defence systems, Doppler Navigation aids, Satellite Navigation systems, etc [483].

The designing and analysis of crescent shaped UWB dipole antenna structure led to the conclusion that the impedance matching complexities can be minimized and bandwidth can be further enhanced by designing dipole structures. It is also concluded that the impedance bandwidth can be enhanced by increasing the number of edges of the radiating dipole arms i.e. achieving the circular or elliptical shape of radiator and the impedance matching can be improved by notch loading. In the upcoming chapter, the major contributions made in this thesis, conclusion drawn during the whole investigation and future scope are summarized.